PCCP

PAPER

View Article Online
View Journal | View Issue

Check for updates

Cite this: *Phys. Chem. Chem. Phys.*, 2022, **24**, 9943

# Terahertz spectroscopy of the helium endofullerene He@$C_{60}$

Tanzeeha Jafari,[a] George Razvan Bacanu,[b] Anna Shugai,[a] Urmas Nagel,[a] Mark Walkey,[b] Gabriela Hoffman,[b] Malcolm H. Levitt,[b] Richard J. Whitby[b] and Toomas Rõõm*[a]

Received 31st January 2022,
Accepted 3rd April 2022

DOI: 10.1039/d2cp00515h

rsc.li/pccp

We studied the quantized translational motion of single He atoms encapsulated in molecular cages by terahertz absorption. The temperature dependence of the THz absorption spectra of $^3$He@$C_{60}$ and $^4$He@$C_{60}$ crystal powder samples was measured between 5 and 220 K. At 5 K there is an absorption line at 96.8 cm$^{-1}$ (2.90 THz) in $^3$He@$C_{60}$ and at 81.4 cm (2.44 THz) in $^4$He@$C_{60}$, while additional absorption lines appear at higher temperature. An anharmonic spherical oscillator model with a displacement-induced dipole moment was used to model the absorption spectra. Potential energy terms with powers of two, four and six and induced dipole moment terms with powers one and three in the helium atom displacement from the fullerene cage center were sufficient to describe the experimental results. Excellent agreement is found between potential energy functions derived from measurements on the $^3$He and $^4$He isotopes. One absorption line corresponds to a three-quantum transition in $^4$He@$C_{60}$, allowed by the anharmonicity of the potential function and by the non-linearity of the dipole moment in He atom displacement. The potential energy function of icosahedral symmetry does not explain the fine structure observed in the low temperature spectra.

Open Access Article. Published on 21 April 2022. Downloaded on 8/26/2025 12:40:34 AM.
This article is licensed under a Creative Commons Attribution 3.0 Unported Licence.

## 1 Introduction

The highly symmetric fullerene, $C_{60}$, has attracted considerable attention since its discovery in 1985.[1] One of the fascinating features is its ability to hold an atom or small molecule within a hollow molecular cavity, forming a complex known as an endofullerene. The discovery of the first endofullerene, La@$C_{60}$, occurred soon after by the same group of researchers, when they were able to capture lanthanum by a laser ablation technique.[2] Endofullerenes provide a rare opportunity to examine the behavior of guest species under conditions that have never been studied before such as the confinement of guest species inside a nano-scale cage which is non-polar, homogeneous and in the case of $C_{60}$, highly symmetric.[3,4]

Different methods have been used to synthesize endofullerenes. Endofullerenes may be synthesized by the arc discharge method in which carbon is evaporated at high temperature in the presence of a metal[5] or an inert gas.[6,7] Insertion of atoms into the fulllerene cage is possible by exposing the fullerene to high temperatures and high pressures of inert gas[8] or by ion bombardment.[9–11] However, these methods are not suited to capture small molecules and the production yield is small. In a major development, the group of Komatsu[12] synthesized $H_2$@$C_{60}$ endofullerenes by a process known as molecular surgery.[13] Following in the footsteps of Komatsu, the group of Murata successfully encapsulated a water molecule inside $C_{60}$.[14] Molecular surgery has been the most successful process to produce high-yield endofullerenes until today. A large number of endofullerenes are now available in macroscopic quantities, such as[12] and its isotopologues,[15] $H_2O$@$C_{60}$,[14] HF@$C_{60}$[16] and $CH_4$,[17] and atoms like Ar,[18] He[19,20] and Ne.[20]

Endofullerenes are of great interest due to quantum effects which are more evident at cryogenic temperatures. The encapsulation isolates atoms and molecules from each other preventing them from forming liquid or solid condensates even at the lowest temperatures. This provides a unique opportunity to study their internal degrees of freedom at the lowest temperatures. The translational motion becomes quantized due to the confining potential. The confinement also prompts the coupling of translational and rotational motions of the encapsulated molecule. The combination of small molecular mass and tight confinement inside the nano cage gives rise to a discrete and well separated translation-rotational energy level structure. The most studied endohedral complex is $H_2$@$C_{60}$, which laid the basis for understanding the quantum dynamics of the isolated systems.[4,21] Different spectroscopic techniques have been used to demonstrate the effect of the highly symmetric trapping potential on the quantum dynamics of the hydrogen

[a] *National Institute of Chemical Physics and Biophysics, Akadeemia tee 23, Tallinn 12618, Estonia. E-mail: toomas.room@kbfi.ee*
[b] *School of Chemistry, University of Southampton, SO17 1BJ Southampton, UK*

Open Access Article. Published on 21 April 2022. Downloaded on 8/26/2025 12:40:34 AM.
This article is licensed under a Creative Commons Attribution 3.0 Unported Licence.

molecule, including infrared spectroscopy (IR)[22–24] and inelastic neutron scattering (INS).[25–28]

There is a growing interest in extending spectroscopic studies to noble gas endofullerenes. The research interest in noble gas endofullerenes is evident from the theoretical studies that have been done so far.[29–36] The incarceration of large noble gas atoms results in the structural and electronic distortion of which has been examined by IR and Raman,[34] NMR,[37] X-ray[38] and electronic spectroscopy.[39]

The first experimental evidence of a noble gas endofullerene was He@$C_{60}$. It was spotted by mass spectrometry when the 4 atom was incorporated in $C_{60}$ as the highly accelerated $C_{60}^{+}$ ions struck with helium gas[9] and later found in fullerenes produced by arc discharge in the He gas.[6] Despite that, and the 2010 synthesis of He@$C_{60}$ by molecular surgery,[19] the He endofullerene potential energy function study was restricted to theoretical explanations[31,33,40] and the experimental data were inadequate for supporting the available information. Recently, the translational energies of He@$C_{60}$ were determined by inelastic neutron scattering and THz spectroscopy studies and the experimentally derived potential was compared to estimates from quantum chemistry calculations and from sums of empirical two-body potentials.[41]

Here, as compared to ref. 41, we present a more detailed temperature-dependence study of THz absorption by endohedral 3 and 4 isotopes between 5 and 220 K. Also, we obtained a better fit of line intensities by including an $r^3$ term in the expansion of the dipole moment in the helium atom displacement $r$. The temperature dependence and the new fit of line intensities confirms the assignment of the He atom translational energy levels and the accuracy of the derived potential energy surface reported in our previous paper.[41]

# 2 Theory

The potential energy surface of the He atom stems from its interaction with the interior of the $C_{60}$ molecule. Although the molecule has icosahedral symmetry we approximate it by spherical symmetry. Within this approximation we may ignore the coupling of the $C_{60}$ rotations and librations to the He motion. Since the masses of and $C_{60}$ He are different by two orders of magnitude, $M_{C60} \gg M_{He}$, we assume that the $C_{60}$ center of the mass position is not affected by the motion of $C_{60}$ the He atom. Also, we ignore the effect of translational motion of in the crystal lattice and its molecular vibrations. Thus, in this model the He atom moves in a spherically symmetric rigid potential well. This motion can be described by the harmonic spherical oscillator model[42–44] where the coordinate **r** is the displacement of He center of mass from the $C_{60}$ center of mass. To obtain agreement with the observed THz spectra, we add anharmonic corrections to the harmonic potential function. This makes the separation of energy levels non-equidistant.

In general, a free He atom does not absorb electromagnetic radiation at THz frequencies due to the lack of an electric dipole moment. However, similar to the encapsulated hydrogen molecule,[15,22,23] He atoms acquire a dipole moment from the interaction with the inner surface of $C_{60}$. This interaction is modulated by the translational motion of the He atom causing the translational modes to become THz-active.

## 2.1 Anharmonic spherical oscillator

The Hamiltonian $\hat{H}$ for one helium trapped in a spherical potential well is given as

$$\hat{H} = \hat{H}_0 + \hat{V}', \tag{1}$$

where

$$\hat{V}' = V_4 r^4 + V_6 r^6 \tag{2}$$

is the perturbation (anharmonic term) added to the harmonic spherical oscillator Hamiltonian[44]

$$\hat{H}_0 = \frac{p^2}{2M_{He}} + V_2 r^2. \tag{3}$$

The harmonic Hamiltonian has eigenstates

$$|n,\ell,m\rangle = R_{n\ell}(r)Y_{\ell m}(\theta,\phi), \tag{4}$$

where $r \in \{0,\infty\}$, $\theta \in \{0,\pi\}$ and $\phi \in \{0,2\pi\}$. The angular part of each wavefunction $m$ is an ortho-normalized spherical harmonic,

$$\int_0^{2\pi} \mathrm{d}\phi \int_0^{\pi} \sin\theta \,\mathrm{d}\theta [Y_{\ell' m'}(\theta,\phi)]^* Y_{\ell m}(\theta,\phi) = \delta_{\ell\ell'}\delta_{mm'}, \tag{5}$$

with the Condon and Shortley phase convention[45]

$$Y^*_{\ell m}(\theta,\phi) = Y_{\ell m}(\theta,-\phi) = (-1)^m Y_{\ell,-m}(\theta,\phi). \tag{6}$$

The radial wavefunction is[42]

$$R_{n\ell}(r) = C(n,\ell,\xi)\mathrm{e}^{\frac{-\xi r^2}{2}}(\xi r^2)^{\frac{\ell}{2}} L_{\frac{n-\ell}{2}}^{\ell+\frac{1}{2}}[\xi r^2], \tag{7}$$

where $L_n^{\alpha}[x]$ is generalised Laguerre polynomial and $\xi = M_{He}\omega_T\hbar^{-1}$. The radial part of the wavefunction is normalised by the constant

$$C(n,\ell,\xi) = \sqrt{\frac{2\left(\frac{n-\ell}{2}\right)!}{\left(\frac{n+\ell+1}{2}\right)!}}\xi^{\frac{3}{4}}. \tag{8}$$

The eigenenergies of the harmonic Hamiltonian (3) are

$$E_n = \hbar\omega_T\left(n+\frac{3}{2}\right), \tag{9}$$

where the angular frequency is

$$\omega_T = \sqrt{\frac{2V_2}{M_{He}}}. \tag{10}$$

The problem can be solved by diagonalizing the Hamiltonian (1) using the basis set of functions (4) where $n \in \{0, 1,\ldots, n_{max}\}$. The angular momentum quantum number $\ell$ is given by $\ell \in \{0, 2\ldots n\}$ for even $n$ and $\ell \in \{1, 3\ldots n\}$ for odd $n$.

 This journal is © the Owner Societies 2022

Open Access Article. Published on 21 April 2022. Downloaded on 8/26/2025 12:40:34 AM. This article is licensed under a Creative Commons Attribution 3.0 Unported Licence.

It is practical to use the reduced matrix elements, $\langle \ell_f \| T_k \| \ell_i \rangle$, of the spherical tensor operator $T_{kq}$ of rank $k$, $q \in \{-k, -k+1, \ldots, k\}$, which are independent of $m$ and $q$.[46] The matrix element of $T_{kq}$ is

$$\langle \tau_f, \ell_f, m_f | T_{kq} | \tau_i, \ell_i, m_i \rangle = (-1)^{\ell_f - m_f} \begin{pmatrix} \ell_f & k & \ell_i \\ -m_f & q & m_i \end{pmatrix} \langle \tau_f, \ell_f \| T_k \| \tau_i, \ell_i \rangle, \quad (11)$$

where the angular part of the reduced matrix element is

$$\langle \ell_f \| T_k \| \ell_i \rangle = (-1)^{\ell_f} \sqrt{\frac{(2\ell_f+1)(2k+1)(2\ell_i+1)}{4\pi}} \begin{pmatrix} \ell_f & k & \ell_i \\ 0 & 0 & 0 \end{pmatrix}. \quad (12)$$

The six symbols in the brackets denote the Wigner 3*j*-symbol. The 3*j*-symbol is zero if conditions $|\ell_f - \ell_i| \le k \le \ell_f + \ell_i$ and $m_f + q + m_i = 0$ are not satisfied; if $m_f = q = m_i = 0$, then the 3*j*-symbol is not zero if the sum $\ell_f + k + \ell_i$ is an even number.[46]

For the isotropic spherical potential, eqn (2), the rank of potential spherical operator is $k = 0$. Therefore, the states with different $\ell$ and $m$ are not mixed. Perturbation $V_N r^N$ mixes states with different $n$ and the eigenstate of Hamiltonian (1), $|\tau,\ell,m\rangle$, is a linear superposition of states $|n,\ell,m\rangle$, eqn (4). Evaluation of matrix elements of the radial part of harmonic oscillator wavefunction, $\langle R_{n_f \ell_f} | r^N | R_{n_i \ell_i} \rangle$ with $\ell_f = \ell_i$, shows that non-zero elements are $|n_f - n_i| \le N$ where $n_i$ and $n_f$ must have the same parity. Because each energy level of the anharmonic Hamiltonian (1) is $(2\ell + 1)$-fold degenerate in $m$, it is sufficient to include only the $|n,\ell,0\rangle$ functions in the basis set. This reduces the number of states by a factor $2\ell + 1$ for each $\ell$.

### 2.2 THz absorption line strengths of the spherical oscillator

We write the dipole moment in spherical harmonics $Y_{1q}(\theta,\phi)$ as a function of He displacement keeping the first two terms, linear and cubic in $r$,

$$d_{1q} = \sqrt{\frac{4\pi}{3}} \left( A_{1,1q} r + A_{3,1q} r^3 \right) Y_{1q}(\theta,\phi), \; q \in \{-1, 0, +1\}. \quad (13)$$

Only the odd powers of $r$ are present because the dipole moment is a polar vector. $A_{1,1q}$ and $A_{3,1q}$ are the amplitude coefficients. In the spherical symmetry the amplitudes do not depend on $q$, and we use a simplified notation, $A_{1,1q} \equiv A_1$ and $A_{3,1q} \equiv A_3$. The length of the dipole moment vector is $|\mathbf{d}| = \sqrt{\sum_{q=-1}^{+1} (d_{1q})^* d_{1q}} = A_1 r + A_3 r^3$, as follows from the normalization of spherical harmonics, $\sum_{m=-\ell}^{\ell} Y^*_{\ell m}(\theta,\phi) Y_{\ell m}(\theta,\phi) = \frac{2\ell+1}{4\pi}$.

Using the Fermi golden rule we write the THz absorption line area for the radiation polarized linearly in the $z$ direction, which couples to the dipole moment $z$ component, $d_z = d_{10}$. Since the energy $E$ of Hamiltonian (1) is degenerate in initial and final state quantum numbers $m$ we perform the summation over $m_i$ and $m_f$ for a given transition frequency, $\omega_{fi} = (E_f - E_i)/hc_0$. The absorption line area $S_{fi}$ is

$$S_{fi} = \int_{\omega_{fi}} \alpha_{fi}(\omega) d\omega = \mathcal{N} f_0 \frac{2\pi^2}{h\varepsilon_0 c_0 \eta} \left( \frac{\eta^2+2}{3} \right)^2 \omega_{fi} (p_i - p_f) \times \sum_{m_i, m_f} |\langle \tau_f, \ell_f, m_f | d_{10} | \tau_i, \ell_i m_i \rangle|^2, \quad (14)$$

where the integral is taken over the frequency range $\omega_{fi}$ spanning the transition $|i\rangle \to |f\rangle$. $c_0$ is the speed of light in a vacuum, $\varepsilon_0$ is the permittivity of vacuum, $h$ is the Planck and $k_B$ is the Boltzmann constant. Factor $(\eta^2 + 2)/3$ is the enhancement of radiation electric field at the molecule embedded in dielectric[47] and $\eta$ is the index of refraction (for $\eta = 2$, ref. 48). $\mathcal{N} = 1.48 \times 10^{27}\ \mathrm{m}^{-3}$ is the number density of molecules in the solid and $f_0 = \mathcal{N}_\bullet / \mathcal{N}$ is the filling factor; $\mathcal{N} = \mathcal{N}_\bullet + \mathcal{N}_\circ$ where $\mathcal{N}_\bullet$ is the number density of filled and $\mathcal{N}_\circ$ is the number density of empty cages. All units are SI and the transition frequency, $\omega_{fi}$, is measured in wavenumbers, number of waves in one meter, $[\omega_{fi}] = \mathrm{m}^{-1}$. $p_i$ and $p_f$ are the thermal Boltzmann populations of the initial and final states:

$$p_i = \frac{e^{-E_i/k_B T}}{\sum_j (2\ell_j + 1) e^{-E_j/k_B T}}, \quad (15)$$

where $2\ell_j + 1$ is the degeneracy of state $|\tau_j,\ell_j,m_j\rangle$ in quantum number $m_j$.

The sum over $m_i$ and $m_f$ in eqn (14) is

$$\sum_{m_i, m_f} |\langle \tau_f, \ell_f, m_f | d_{10} | \tau_i, \ell_i, m_i \rangle|^2 = \frac{1}{3} |\langle \tau_f, l_f \| d_1 \| \tau_i, \ell_i \rangle|^2, \quad (16)$$

where $\langle \tau_f, l_f \| d_1 \| \tau_i, \ell_i \rangle$ is the reduced matrix element of $d_{1q}$ with the angular part given by eqn (12). Since for the dipole moment $k = 1$, a selection rule of THz absorption by a spherical oscillator, $\ell_f = \ell_i \pm 1$, follows from the properties of the 3*j*-symbol. The selection rule for $n$ comes from the matrix element of the radial part of harmonic oscillator wavefunction, $\langle R_{n_f \ell_{i\pm1}} | r^N | R_{n_i \ell_i} \rangle$. For the linear term in eqn (13) it is $n_f = n_i \pm 1$ and for the cubic term it is $|n_f - n_i| \le 3$, where $n_i$ and $n_f$ must have different parities.

## 3 Experimental

$^3$He@$C_{60}$ and $^4$He@$C_{60}$ were synthesised using a solid-state process for the critical step, as described in ref. 20. The initial filling factors were 30% to 50%. The samples were further purified by recirculating HPLC on Cosmosil Buckyprep columns to remove trace impurities of $H_2O$@$C_{60}$ and empty $C_{60}$. Finally, the $^4$He@$C_{60}$ sample had a filling factor of $f_0 = (88.2 \pm 0.5)\%$ while the $^3$He@$C_{60}$ had a filling factor of $f_0 = (97.2 \pm 0.5)\%$, as determined by $^{13}$C NMR. Samples were sublimed under vacuum.

The sublimed powdered sample was put inside the 3 mm diameter hole of cylindrical brass frame and pressed under the vacuum into a pellet. The mass and thickness of the $^3$He@$C_{60}$ pellet were 28 mg and 2.16 mm and of the $^4$He@$C_{60}$ pellet were 21 mg and 1.72 mm. The brass frame with the pellet was

Open Access Article. Published on 21 April 2022. Downloaded on 8/26/2025 12:40:34 AM.
This article is licensed under a Creative Commons Attribution 3.0 Unported Licence.

inserted into a sample chamber with two thin-film polypropylene windows and with a vacuum line for pumping and filling with helium heat exchange gas. The sample chamber was in a thermal contact with the cold finger of the cryostat. The cryostat was placed inside the interferometer Vertex 80v sample compartment. The cold finger with the sample chamber was moved up and down by letting the beam through the sample chamber or through a reference hole with 3 mm diameter. The transmission spectra were recorded up to 300 $cm^{-1}$ using a Hg lamp, a 6 μm Mylar beam splitter, and a 4 K bolometer. The spectral resolution was 0.2 $cm^{-1}$ which was found to be smaller than the width of the He absorption lines or their subcomponents.

The absorption spectra were calculated from $\alpha(\omega) = -d^{-1}\ln\left[\mathscr{T}(\omega)\mathscr{R}(\omega)^{-1}\right]$ where $\alpha(\omega)$ is the absorption coefficient, $\mathscr{T}(\omega)$is the transmission, and $\mathscr{R}(\omega)$ is the amount of light lost in reflections from the pellet surfaces and the sample chamber windows. The measured transmission is $\mathscr{T}(\omega) = I_s(\omega)/I_r(\omega)$, where $I_s(\omega)$ is the beam intensity at the bolometer with the sample chamber in the beam and $I_r(\omega)$ is the beam intensity at the bolometer with the reference hole in the beam. The reflection losses and the absorption in the sample chamber windows affect the background absorption but do not affect the absorption line areas of helium.

## 4 Results

The THz absorption spectra of $^3$He@$C_{60}$ and $^4$He@$C_{60}$ at different temperatures in a spectral range between 75 and 150 $cm^{-1}$ are shown in Fig. 1. The baseline of the 5 K spectrum was fitted and then subtracted. The same procedure but covering only the spectral range around the line no. 1 was applied to the spectra of higher temperatures. For the rest of the spectra above the line no. 1 the average of 5 and 15 K spectra was used for the baseline subtraction. The broad line at about 140 $cm^{-1}$ in the 5 K spectrum is the absorption feature of the mylar windows on the sample cell.

The spectra from the two isotopes share the same pattern of absorption spectra but with the $^4$He lines shifted to higher energy relative to the $^4$He lines. The line intensities of the two isotopes are similar. For $^3$He, a line at 97 $cm^{-1}$ is the only line present at 5 K and its intensity decreases with increasing temperature. This indicates that it corresponds to a transition from the ground state. With the rise in temperature, energy levels above the ground state become thermally populated and we observe six more absorption lines: 106, 114, 120, 122, 128 and 138 $cm^{-1}$.

In the case of $^4$He@$C_{60}$, we observed two transitions from the ground state, at 81 $cm^{-1}$ and at 284 $cm^{-1}$. By increasing the temperature additional absorption lines become visible at 88, 95, 101, 106, 111, 114 and 126 $cm^{-1}$. The line no. 9 starts from the ground state as is confirmed by its $T$ dependence, Fig. 7 in the Appendix. This line cannot be detected in $^3$He@$C_{60}$ THz spectra because of the strong absorption by the fullerene at its resonance frequency, 340.6 $cm^{-1}$ in Table 4, but was observed in the inelastic neutron scattering spectrum, line no. $e$ in ref. 41.

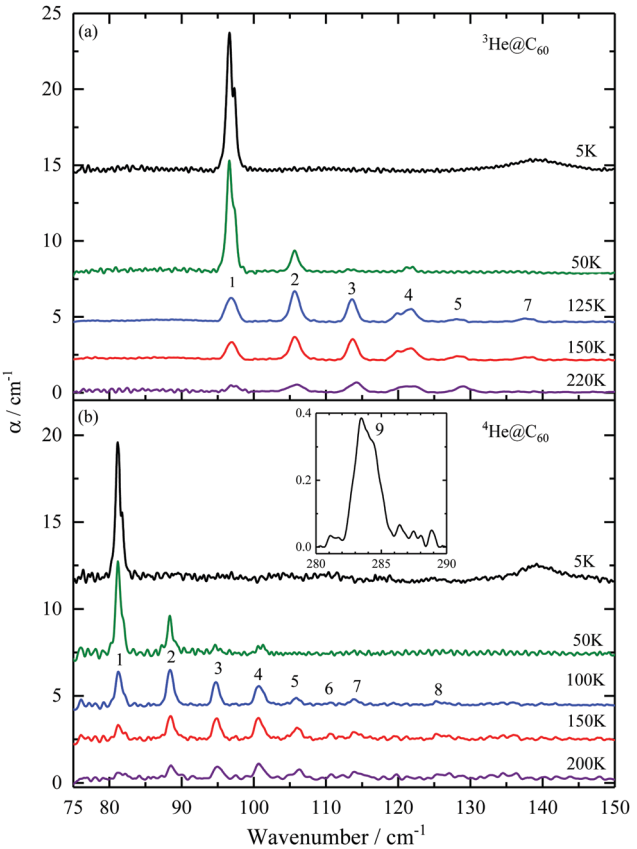


Fig. 1 Temperature dependence of THz absorption spectra of $^3$He@$C_{60}$ (a) and $^4$He@$C_{60}$ (b). Absorption lines are numbered according to the transitions between the energy levels as shown in Fig. 3. Inset to (b) shows the $^4$He@$C_{60}$ line no. 9 at 5 K. The line intensities are not corrected for the filling factor $f_0$, see eqn (14).

The lowest energy peak has a two-component structure which is visible at low temperatures. The separation of components is approximately 0.8 $cm^{-1}$ for $^3$He@$C_{60}$ and 0.7 $cm^{-1}$ for $^4$He@$C_{60}$, Tables 4 and 5 in the Appendix. We did not see any additional structure at the best resolution we used, 0.2 $cm^{-1}$. The possible origin of line no. 1 and no. 9 splitting is discussed in Section 5.

The synthetic spectra were fitted with a spherical oscillator model, as described in the Appendix, and the result is shown in Fig. 2. The best spherical oscillator model fit parameters are listed in Table 2. As compared to our previous fit[41] the extra term, $A_3r^3$, was added to the dipole moment expansion, eqn (13). This gives a better fit of the line intensities. The spherical oscillator fit revealed that line number 4 consists of three closely spaced transitions, and lines 5 and 6 of two transitions. The energy diagram together with the numbered transitions is shown in Fig. 3 and the energies of corresponding levels in Table 2. The list of line frequencies and intensities calculated with the spherical oscillator model best fit parameters for $^3$He (125 K) and $^4$He (100 K) is given in the Appendix, Tables 4 and 5.

 This journal is © the Owner Societies 2022

Open Access Article. Published on 21 April 2022. Downloaded on 8/26/2025 12:40:34 AM.
This article is licensed under a Creative Commons Attribution 3.0 Unported Licence.

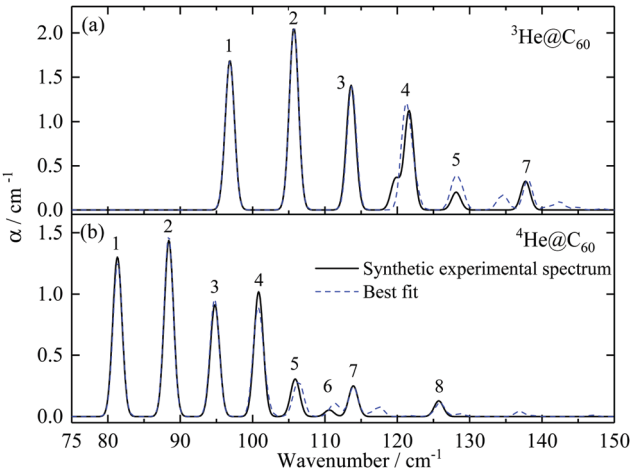


Fig. 2 Synthetic experimental THz spectrum (solid black line) and the best fit result (blue dashed line) of $^3$He@C$_{60}$ at 125K (a) and $^4$He@C$_{60}$ at 100 K (b).

In Fig. 4 the areas of the first five THz absorption lines of $^3$He@C$_{60}$ and $^4$He@C$_{60}$ are compared with the temperature dependence of line areas derived from the spherical oscillator model fit. The line areas at each temperature are calculated using the parameters $\{V_2,V_4,V_6,A_1,A_3\}$ obtained from the anharmonic oscillator model fit of 125 K and 100 K spectra of $^3$He and $^4$He, respectively. For each line the line areas are normalized to the maximum of the theoretical intensity *versus* temperature curve. Same normalization factors are applied to each experimental line respectively.

## 5 Discussion

The overlap of potential energy curves of two He isotopes proves the reliability of our fit as the difference of potential curves is only about $\pm 0.5$ cm$^{-1}$ over the energy scale probed by THz spectroscopy, Fig. 5(b). The potential is strongly anharmonic. It can be seen that for the displacement $r > 75$ pm the anharmonic contribution to the potential energy, $V_4r^4 + V_6r^6$, starts to dominate over the harmonic part, $V_2r^2$. The significance of anharmonic correction is also evidenced by the composition of the oscillator wave function: as the energy increases the single $n$-component of a wavefunction becomes less dominant meaning that the components with other $n$ values are mixed in Table 2. States with different $\ell$ values are not mixed by the isotropic potential and each level is $2\ell + 1$ degenerate in the quantum number $m$.

Experimentally determined translational energies of $A$@C$_{60}$ endohedral complexes are summarized in Table 3. Although the anharmonic contributions to the potential have been determined experimentally,[15,22,23] a more detailed comparison with is not meaningful as firstly, has translation–rotation coupling terms in the potential and secondly, it misses the $V_6$ term in the potential fit. The shape of the potential curve is not known for other $A$ species. We approximate the translational energy, $\omega_T$, as the difference of energies between the ground

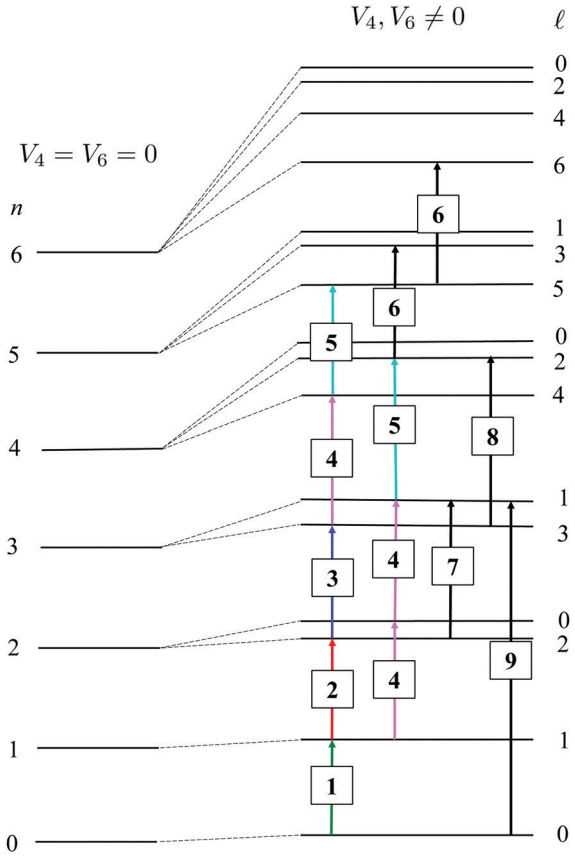


Fig. 3 Energy level diagram and THz transitions of He@C$_{60}$. The principal translational quantum number is $n$ and the angular momentum quantum number is $\ell$. The energy levels of a spherical harmonic oscillator are degenerate in $\ell$, shown on left. The anharmonic terms in the potential, and $V_6$, split the energy levels with different $\ell$ and each energy level has the unique $\ell$ value within the spherical symmetry, on the right. The mixing of states with different $n$ by $V_4$ - and $V_6$ -term is not shown on the diagram. The THz transitions between the translational energy levels observed in the experiment are labeled with numbers, see Fig. 1 and Tables 4 and 5, and the translational energies are in Table 2.

state and the first excited translational state,. Assuming harmonic approximation, $V_2^A \approx M_A{\omega_{01}}^2/2$, we scaled the potential of other species, $V_2^A$, relative to hydrogen, ${V_2}^H$. The last column demonstrates that $1/\sqrt{M_A}$ scaling of translational frequency of different $A$ species has no predictive power. In general, the interaction of neutral $A$ with can be separated into repulsive interaction and electrostatic interaction expanded in induction and dispersion terms.[33] Since has no electric dipole nor quadrupole moment the induction terms are zero. The absence of induction terms may only partially explain the ''softness'' of potential because the dominant interactions are repulsion and dipole–dipole dispersion for endohedral atoms and molecules.[33] In general, modern quantum chemistry calculations of He@C$_{60}$ give a good description of $V(r)$.[41]

To further validate the potential parameters of obtained from the fit of single high temperature spectra we compare the temperature dependence of line intensities of measured and calculated spectra, Fig. 4. The parameters determined from

Open Access Article. Published on 21 April 2022. Downloaded on 8/26/2025 12:40:34 AM.
This article is licensed under a Creative Commons Attribution 3.0 Unported Licence.

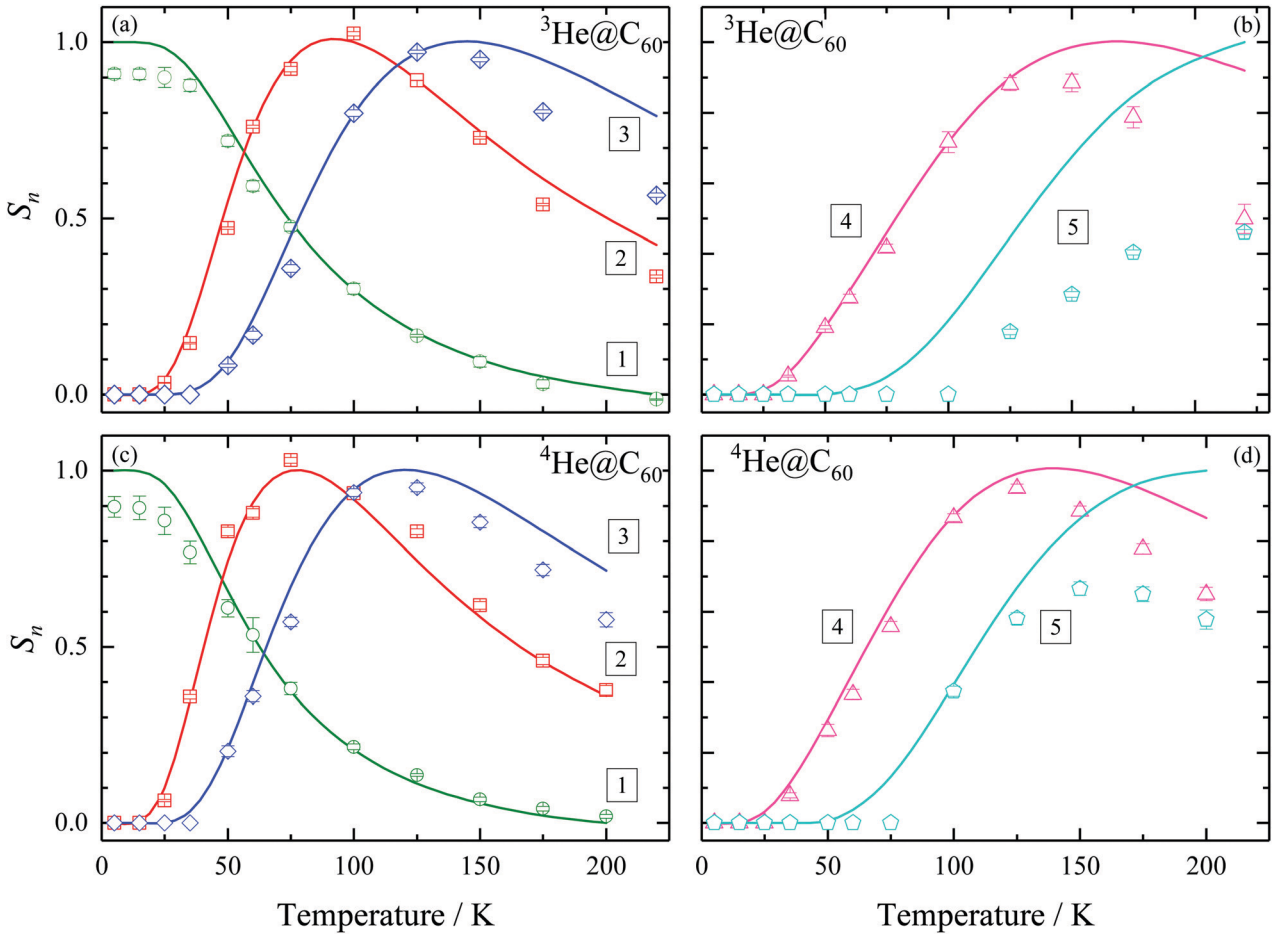


Fig. 4 Temperature dependence of normalized THz absorption lines areas $S_n$ of $^3$He@C$_{60}$, panels (a) and (b) and of $^4$He@C$_{60}$, panels (c) and (d). Symbols are experimental line areas with errors from the fit with Gaussian lines and solid lines are theoretical areas calculated with the parameters from Table 1. Line areas have been normalized to the maximum value in the $T$ dependence of theoretical area for each line. The lines are numbered according to the transitions shown in Fig. 3 and listed in Tables 4 and 5.

the $^3$He ($^4$He) fit at 125 K (100 K) describe the temperature dependence from 5 to 200 K rather well except for the line no. 5. Other lines, no. 6, no. 7, no. 8 and no. 9, are weak and their intensities could not be determined reliably from the experimental spectra and therefore their $T$ dependence was not analyzed. The intensity of the lowest frequency line no. 1, transition from the ground state, is overestimated by the fit at the lowest temperatures. The discrepancy of calculated and measured $T$ dependence could be due the thermal motion of C$_{60}$ not taken into account in our model.

The dipole moment of is induced by the displacement from the C$_{60}$ cage center. The estimate for the displacement of the first transition can be made from the potential energy which is half of the total energy, $V(r) = E_1/2$. Using the data from Table 2, $E_1 = 222.5$ cm$^{-1}$ ($^3$He) and $E_1 = 187.9$ cm$^{-1}$ ($^4$He), we obtain the displacement to be about 60 pm. The dipole moment induced by 60 pm displacement is $d = A_1 r + A_3 r^3 = 2.7 \times 10^{-2}$ D, small compared to permanent dipole moments of molecules. For example, the permanent screened dipole moment of C$_{60}$ endohedral water is about 0.5 D.[49,50]

Transition no. 9 starts from the ground state with $\ell = 0$ and predominantly with $n = 0$ radial content. The final state is the $\ell = 1$ state, see Fig. 3 and Table 2, but with predominantly $n = 3$ radial part. It is an allowed electric dipole transition with the selection rule $\Delta\ell = +1$ but three translation quanta are created, $\Delta n = +3$. All other lines, no. 1 to no. 8, are ordinary one quantum transitions, $\Delta n = +1$. The $r^3$ term in the dipole moment expansion allows the $\Delta n = +3$ excitation by radiation. However, because of the mixing of states by anharmonic potential, $n = 0$ state is mixed with $n = 2$ and $n = 3$ state is the mixed $n = 1$ state, the linear term in $r$ of the dipole moment expansion with the selection rule $\Delta n = +1$ can induce the three-quantum transition. Thus, in there are two factors what activate the three-quantum transition, the anharmonicity of the potential and the $r^3$ term in the dipole moment expansion.

Two absorption lines, no. 1 and no. 9, show partially resolved fine structure at 5 K, Fig. 1. These lines are the transitions from the ground state with $\ell = 0$ to the state $\ell = 1$, see Fig. 3 and Table 2. In the icosahedral potential the first $A_g$ symmetry representation after fully spherical potential, rank $k = 0$, is a combination of spherical harmonics of rank $k = 6$.[51] Rank 6 term in the potential splits states with $\ell \geq 3$, which cannot explain the fine structure of helium line no. 1 and no. 9.

 This journal is © the Owner Societies 2022

Open Access Article. Published on 21 April 2022. Downloaded on 8/26/2025 12:40:34 AM.
This article is licensed under a Creative Commons Attribution 3.0 Unported Licence.

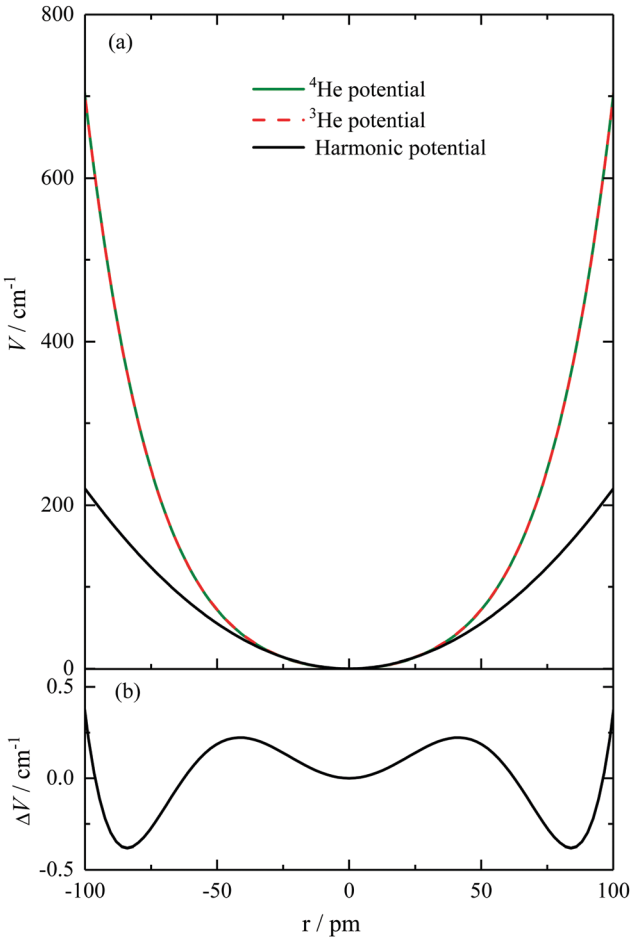


Fig. 5 (a) Potential energy curves of $^3$He and $^4$He, $V(r) = V_2r^2 + V_4r^4 + V_6r^6$, calculated with parameters from Table 1. The harmonic part of $^3$He potential curve, $V_2r^2$, is plotted as blue solid line. The potential curves of two isotopes, green solid line of $^3$He and red dashed line of $^3$He, are indistinguishable in this plot. (b) The difference between the potential curves of $^3$He and $^4$He, $\Delta V = V_3 - V_4$, is less than $\pm 0.5$ cm$^{-1}$.

Table 1 The best fit parameter values for $^3$He@C$_{60}$ and $^4$He@C$_{60}$. $V_2$, $V_4$ and $V_6$ are potential parameters, eqn (2) and (3), and $A_1$ and $A_3$ are the dipole moment parameters, eqn (13)

| $\kappa_i$ | $^3$He@C$_{60}$ | $^4$He@C$_{60}$ | Unit |
|---|---|---|---|
| $V_2$ | $(2.500 \pm 0.015) \times 10^{-3}$ | $(2.46 \pm 0.04) \times 10^{-3}$ | meV pm$^{-2}$ |
| $V_4$ | $(3.64 \pm 0.03) \times 10^{-7}$ | $(3.77 \pm 0.08) \times 10^{-7}$ | meV pm$^{-4}$ |
| $V_6$ | $(2.560 \pm 0.017) \times 10^{-11}$ | $(2.46 \pm 0.06) \times 10^{-11}$ | meV pm$^{-6}$ |
| $A_1$ | $(3.83 \pm 0.10) \times 10^{-4}$ | $(3.73 \pm 0.22) \times 10^{-4}$ | D pm$^{-1}$ |
| $A_3$ | $(1.7 \pm 0.3) \times 10^{-8}$ | $(2.3 \pm 0.6) \times 10^{-8}$ | D pm$^{-3}$ |

Table 2 Translational energy levels of $^3$He@C$_{60}$ and $^4$He@C$_{60}$ obtained from the fit of THz absorption spectra. Translational energy $E$, the angular momentum quantum number $\ell$ (single-valued for each energy level), and the amplitude squared of the main component of eigenstate with the principal quantum number $n$. The zero point energy 125.7 cm$^{-1}$ (106.5 cm$^{-1}$) of $^3$He ($^4$He) has been subtracted

| $^3$He@C$_{60}$ | | | | $^4$He@C$_{60}$ | | | |
|---|---|---|---|---|---|---|---|
| $E$/cm$^{-1}$ | $\ell$ | $n$ | $\lvert\xi_n\rvert^2$ | $E$/cm$^{-1}$ | $\ell$ | $n$ | $\lvert\xi_n\rvert^2$ |
| 0 | 0 | 0 | 0.95 | 0 | 0 | 0 | 0.95 |
| 96.8 | 1 | 1 | 0.87 | 81.4 | 1 | 1 | 0.88 |
| 202.6 | 2 | 2 | 0.77 | 169.8 | 2 | 2 | 0.79 |
| 218.3 | 0 | 2 | 0.64 | 182.1 | 0 | 2 | 0.68 |
| 316.3 | 3 | 3 | 0.65 | 264.5 | 3 | 3 | 0.69 |
| 340.6 | 1 | 3 | 0.43 | 283.7 | 1 | 3 | 0.48 |
| 437.3 | 4 | 4 | 0.54 | 365.1 | 4 | 4 | 0.58 |
| 469.4 | 2 | 6 | 0.39 | 390.6 | 2 | 6 | 0.39 |
| 483.0 | 0 | 6 | 0.40 | 401.1 | 0 | 6 | 0.40 |
| 565.1 | 5 | 5 | 0.43 | 471.1 | 5 | 5 | 0.47 |
| 604.3 | 3 | 7 | 0.36 | 502.0 | 3 | 7 | 0.38 |
| 625.8 | 1 | 7 | 0.31 | 519.0 | 1 | 7 | 0.35 |
| 699.3 | 6 | 8 | 0.37 | 582.2 | 6 | 6 | 0.38 |
| 745.1 | 4 | 10 | 0.29 | 618.2 | 4 | 8 | 0.31 |
| 774.0 | 2 | 10 | 0.30 | 640.8 | 2 | 10 | 0.30 |
| 787.4 | 0 | 10 | 0.30 | 650.5 | 0 | 10 | 0.31 |

Table 3 The translational energies of endohedral species $A$ in $A$@C$_{60}$ from the ground to the first excited state, $\hbar\omega_{01}$. The scaling of $V_2^A$ with respect to $V_2^{H_2}$ is found using harmonic approximation, $\omega_T = \omega_{01}$, and eqn (10) where $M_A$ is the mass in atomic mass units, a.u

| $A$ | $\hbar\omega_{01}$/cm$^{-1}$ | $M_A$/a.u. | $V_2^A/V_2^{H_2}$ |
|---|---|---|---|
| $H_2$ | 179.5[23] | 2 | 1 |
| $^3$He | 96.7[41] | 3 | 0.44 |
| $^4$He | 81.3[41] | 4 | 0.41 |
| HF | 78.6[16] | 20 | 1.92 |
| $H_2O$ | 110[49] | 18 | 3.4 |

To explain the spectral line splitting, a potential with symmetry lower than the icosahedral or two different exohedral environments must be invoked.

Fullerene molecules stop rotating below 90 K.[52] This leads to two sites distinguished by the relative orientation of the central cage and its 12 nearest-neighbor C$_{60}$.[53] In the pentagonal orientation the electron-rich double bonds are facing pentagonal rings and in the hexagonal orientation the electron-rich double bonds are facing hexagonal rings of nearest-neighbor cages. It was proposed by Felker *et al.*[54] that the orientational order creates electrostatic field that interacts with the quadrupole moment of endohedral molecule. Their model explains the splitting of $J = 1$ rotational state observed in $H_2$@C$_{60}$,[22,23,28] HF@C$_{60}$[16] and $H_2O$@C$_{60}$.[49,55,56] This mechanism is not applicable to the helium atom because it does not have rotational degrees of freedom nor quadrupole moment. The icosahedral symmetry of $V(r)$ could still be disturbed by the nearest-neighbor C$_{60}$ molecules. A splitting similar to the splitting of line no. 1 was observed in $H_2$@C$_{60}$ for the $\ell = 0 \rightarrow \ell = 1$ transition of *para*-$H_2$@C$_{60}$ in the $J = 0$ rotational state.[22,23] Application of pressure changes the relative population of pentagon- and hexagon-oriented molecules.[57] The analysis of the inelastic neutron scattering spectra of pressure-treated $H_2$@C$_{60}$ shows that the potential and the energy levels of are sensitive to the orientation of neighboring cages.[28] Similar THz and infrared spectroscopy experiments are planned to verify the effect of orientational order on the potential energy function of endohedral molecules and atoms in C$_{60}$.

In summary, with the THz absorption spectroscopy we have determined the energy level structure of quantized

Open Access Article. Published on 21 April 2022. Downloaded on 8/26/2025 12:40:34 AM.
This article is licensed under a Creative Commons Attribution 3.0 Unported Licence.

translational motion of single $^3$He and $^4$He atoms trapped in the $C_{60}$ molecular cages. The fitted potential energy curves and the induced dipole moments of two isotopes overlap with high precision. However, there are deviations between the modeled and measured spectra. Firstly, the fine structure of spectral lines observed in the low temperature spectra cannot be explained by icosahedral symmetry of $C_{60}$ molecule. Secondly, there are some discrepancies between the measured and modeled spectra in the line intensities and their temperature dependence. Both deviations could be due to the orientational order and the thermal motion of $C_{60}$ molecules in the solid.

## Conflicts of interest

There are no conflicts to declare.

## Appendix

## Fit of anharmonic spherical oscillator and dipole moment parameters

The experimental THz absorption spectrum was fitted using Gaussian line shapes to find the line areas, line widths and frequencies, see Fig. 6. A synthetic experimental spectrum $y(\omega_n)$, the distance between the points in the spectrum $\omega_n - \omega_{n-1} = \Delta\omega/4$, was then generated consisting of lines with equal full width at half maximum, $\Delta\omega = 1.5$ cm$^{-1}$, while keeping the line areas and frequencies of the original experimental lines. The synthetic spectrum approach was needed as the model did not include any line broadening mechanism.

The synthetic spectra were fitted using the anharmonic spherical oscillator model. The reduced basis was limited to

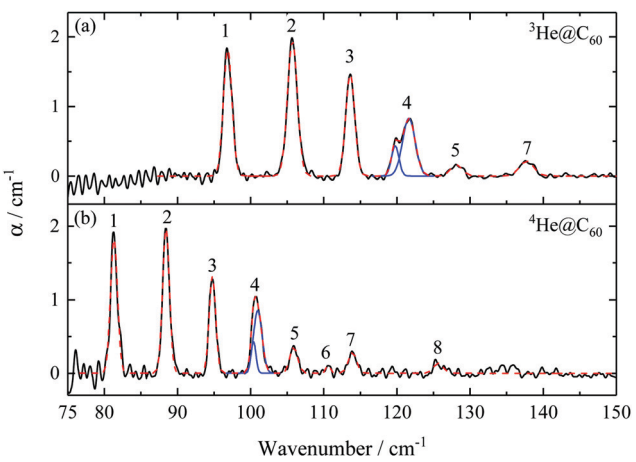


Fig. 6 THz absorption spectrum of $^3$He at 125 K (a) and $^4$He at 100 K (b), black solid line, and the fit with Gaussian lineshapes, blue solid lines. Red dashed line is the sum of Gaussians. The line intensities are not corrected for the filling factor $f_0$, see eqn (14).

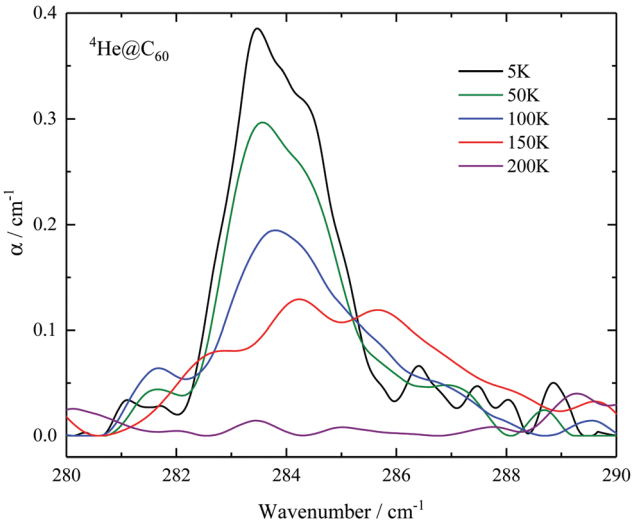


Fig. 7 Temperature dependence of line no. 9 in $^4$He@$C_{60}$.

$n_{max} = 18$ providing 100 states in the reduced basis $|n,\ell\rangle$. For a given model and basis, matrix elements of the Hamiltonian, eqn (1), and the dipole operator, eqn (13), were evaluated analytically in a symbolic form using the Mathematica software. At each step of minimizing chi squared, $\chi^2 = \sum [y - f(\omega_n, \{\kappa\})]^2$, the Hamiltonian was diagonalized numerically. Here $f(\omega_n,\{\kappa\})$ is the theoretical spectrum with the same linewidth and lineshape as the synthetic experimental spectrum; $\{\kappa\} = \{V_2,V_4,V_6,A_1,A_3\}$ is the set of Hamiltonian and dipole operator fit parameters. Errors were calculated using the method described in ref. 49. Adding the $V_6$ term to $V_4$ in the potential reduced $\chi^2$ of $^3$He and $^4$He fit by three and two times, respectively. The frequencies and intensities of experimental spectra and spectra calculated using the best fit parameters are given in Tables 4 and 5.

Table 4 The line frequencies $f$ and areas $S$ of experimental spectra at 5 and 125 K and the anharmonic spherical oscillator model fit results at 125 K for $^3$He@$C_{60}$. The $f$ and $S$ of lines no. 1 and no. 9 at 5 K are calculated using the best fit parameters obtained at 125 K

| | Experiment | | Model fit | |
|---|---|---|---|---|
| Line no. | $f$/cm$^{-1}$ | $S$/cm$^{-2}$ | $f$/cm$^{-1}$ | $S$/cm$^{-2}$ |
| | | 5 K | | |
| 1 | 96.6 | 8.5 | 96.8 | 11.7 |
| | 97.4 | 2.2 | — | — |
| 9 | — | — | 340.6 | 0.4 |
| | | 125 K | | |
| 1 | 96.9 | 2.7 | 96.8 | 2.7 |
| 2 | 105.7 | 3.3 | 105.7 | 3.3 |
| 3 | 113.6 | 2.3 | 113.7 | 2.2 |
| 4 | 119.8 | 0.6 | 121.0 | 1.1 |
| | 121.6 | 1.8 | 121.4 | 0.8 |
| | — | — | 122.4 | 0.5 |
| 5 | 128.1 | 0.3 | 127.8 | 0.5 |
| | — | — | 128.8 | 0.4 |
| 7 | 137.7 | 0.5 | 138.0 | 0.6 |


This journal is © the Owner Societies 2022

Open Access Article. Published on 21 April 2022. Downloaded on 8/26/2025 12:40:34 AM.
This article is licensed under a Creative Commons Attribution 3.0 Unported Licence.

Table 5 The line frequencies $f$ and areas $S$ of experimental spectra at 5 and 100 K and the anharmonic spherical oscillator model fit results at 100 K for $^4He@C_{60}$. The $f$ and $S$ of lines no. 1 and no. 9 at 5 K are calculated using the best fit parameters obtained at 100 K

| | Experiment | | Model fit | |
|---|---|---|---|---|
| Line no. | $f$/cm$^{-1}$ | $S$/cm$^{-2}$ | $f$/cm$^{-1}$ | $S$/cm$^{-2}$ |
| | | 5 K | | |
| 1 | 81.2 | 6.1 | 81.4 | 8.0 |
| | 81.9 | 1.2 | — | — |
| 9 | 283.3 | 0.3 | 283.7 | 0.3 |
| | 284.3 | 0.4 | — | — |
| | | 100 K | | |
| 1 | 81.3 | 2.1 | 81.4 | 2.0 |
| 2 | 88.4 | 2.3 | 88.4 | 2.4 |
| 3 | 94.8 | 1.5 | 94.8 | 1.5 |
| 4 | 100.4 | 0.4 | 100.6 | 0.7 |
| | 101.0 | 1.3 | 100.8 | 0.6 |
| | — | — | 101.6 | 0.3 |
| 5 | 105.9 | 0.5 | 106.0 | 0.3 |
| | — | — | 106.7 | 0.2 |
| 6 | 110.6 | 0.1 | 111.0 | 0.09 |
| | — | — | 111.7 | 0.10 |
| 7 | 113.9 | 0.4 | 113.9 | 0.4 |
| 8 | 125.7 | 0.2 | 125.9 | 0.2 |

## Acknowledgements

This research was supported by the Estonian Ministry of Education and Research institutional research funding IUT23-3, Estonian Research Council grant PRG736, the European Regional Development Fund project TK134 and by EPSRC-UK, grant numbers EP/P009980/1 and EP/T004320/1.

## References

1 H. Kroto, J. Heath, S. O'Brian, R. F. Curl and R. E. Smalley, *Nature*, 1985, **318**, 162–163.
2 J. R. Heath, S. C. O'Brien, Q. Zhang, Y. Liu, R. F. Curl, F. K. Tittel and R. E. Smalley, *J. Am. Chem. Soc.*, 1985, **107**, 7779–7780.
3 M. H. Levitt, *Philos. Trans. R. Soc., A*, 2013, **371**, 20120429.
4 Z. Bačić, *J. Chem. Phys.*, 2018, **149**, 100901.
5 L. Dunsch and S. Yang, *Small*, 2007, **3**, 1298–1320.
6 M. Saunders, H. A. Jiménez-Vázquez, R. J. Cross and R. J. Poreda, *Science*, 1993, **259**, 1428–1430.
7 M. Saunders, H. A. Jiménez-Vázquez, R. J. Cross, S. Mroczkowski, M. L. Gross, D. E. Giblin and R. J. Poreda, *J. Am. Chem. Soc.*, 1994, **116**, 2193–2194.
8 M. Saunders, R. J. Cross, H. A. Jiménez-Vázquez, R. Shimshi and A. Khong, *Science*, 1996, **271**, 1693–1697.
9 T. Weiske, T. Wong, W. Krätschmer, J. K. Terlouw and H. Schwarz, *Angew. Chem., Int. Ed. Engl.*, 1992, **31**, 183–185.
10 T. A. Murphy, T. Pawlik, A. Weidinger, M. Höhne, R. Alcala and J.-M. Spaeth, *Phys. Rev. Lett.*, 1996, **77**, 1075–1078.
11 C. Knapp, N. Weiden, H. Kass, K.-P. Dinse, B. Pietzak, M. Waiblinger and A. Weidinger, *Mol. Phys.*, 1998, **95**, 999–1004.
12 K. Komatsu, M. Murata and Y. Murata, *Science*, 2005, **307**, 238–240.
13 Y. Rubin, T. Jarrosson, G.-W. Wang, M. D. Bartberger, K. N. Houk, G. Schick, M. Saunders and R. J. Cross, *Angew. Chem., Int. Ed.*, 2001, **40**, 1543.
14 K. Kurotobi and Y. Murata, *Science*, 2011, **333**, 613–616.
15 M. Ge, U. Nagel, D. Hüvonen, T. Rõõm, S. Mamone, M. H. Levitt, M. Carravetta, Y. Murata, K. Komatsu, X. Lei and N. J. Turro, *J. Chem. Phys.*, 2011, **135**, 114511.
16 A. Krachmalnicoff, R. Bounds, S. Mamone, S. Alom, M. Concistrè, B. Meier, K. Kouřil, M. E. Light, M. R. Johnson, S. Rols, A. J. Horsewill, A. Shugai, U. Nagel, T. Rõõm, M. Carravetta, M. H. Levitt and R. J. Whitby, *Nat. Chem.*, 2016, **8**, 953–957.
17 S. Bloodworth, G. Sitinova, S. Alom, S. Vidal, G. R. Bacanu, S. J. Elliott, M. E. Light, J. M. Herniman, G. J. Langley, M. H. Levitt and R. J. Whitby, *Angew. Chem., Int. Ed.*, 2019, **58**, 1–7.
18 S. Bloodworth, G. Hoffman, M. C. Walkey, G. R. Bacanu, J. M. Herniman, M. H. Levitt and R. J. Whitby, *Chem. Commun.*, 2020, **56**, 10521–10524.
19 Y. Morinaka, F. Tanabe, M. Murata, Y. Murata and K. Komatsu, *Chem. Commun.*, 2010, **46**, 4532–4534.
20 G. Hoffman, M. C. Walkey, J. Gräsvik, G. R. Bacanu, S. Alom, S. Bloodworth, M. E. Light, M. H. Levitt and R. J. Whitby, *Angew. Chem., Int. Ed.*, 2021, **60**, 8960–8966.
21 M. Xu, F. Sebastianelli, Z. Bačić, R. Lawler and N. J. Turro, *J. Chem. Phys.*, 2008, **128**, 011101.
22 S. Mamone, M. Ge, D. Hüvonen, U. Nagel, A. Danquigny, F. Cuda, M. C. Grossel, Y. Murata, K. Komatsu, M. H. Levitt, T. Rõõm and M. Carravetta, *J. Chem. Phys.*, 2009, **130**, 081103.
23 M. Ge, U. Nagel, D. Hüvonen, T. Rõõm, S. Mamone, M. H. Levitt, M. Carravetta, Y. Murata, K. Komatsu, J. Y.-C. Chen and N. J. Turro, *J. Chem. Phys.*, 2011, **134**, 054507.
24 T. Rõõm, L. Peedu, M. Ge, D. Hüvonen, U. Nagel, S. Ye, M. Xu, Z. Bačić, S. Mamone, M. H. Levitt, M. Carravetta, J. Chen, X. Lei, N. J. Turro, Y. Murata and K. Komatsu, *Philos. Trans. R. Soc., A*, 2013, **371**, 20110631.
25 A. J. Horsewill, K. S. Panesar, S. Rols, M. R. Johnson, Y. Murata, K. Komatsu, S. Mamone, A. Danquigny, F. Cuda, S. Maltsev, M. C. Grossel, M. Carravetta and M. H. Levitt, *Phys. Rev. Lett.*, 2009, **102**, 013001.
26 A. J. Horsewill, S. Rols, M. R. Johnson, Y. Murata, M. Murata, K. Komatsu, M. Carravetta, S. Mamone, M. H. Levitt, J. Y.-C. Chen, J. A. Johnson, X. Lei and N. J. Turro, *Phys. Rev. B: Condens. Matter Mater. Phys.*, 2010, **82**, 081410.
27 A. J. Horsewill, K. S. Panesar, S. Rols, J. Ollivier, M. R. Johnson, M. Carravetta, S. Mamone, M. H. Levitt, Y. Murata, K. Komatsu, J. Y.-C. Chen, J. A. Johnson, X. Lei and N. J. Turro, *Phys. Rev. B: Condens. Matter Mater. Phys.*, 2012, **85**, 205440.
28 S. Mamone, M. R. Johnson, J. Ollivier, S. Rols, M. H. Levitt and A. J. Horsewill, *Phys. Chem. Chem. Phys.*, 2016, **18**, 1998–2005.
29 A. L. R. Bug, A. Wilson and G. A. Voth, *J. Phys. Chem.*, 1992, **96**, 7864–7869.
30 C. Williams, M. Whitehead and L. Pang, *J. Phys. Chem.*, 1993, **97**, 11652–11656.

Open Access Article. Published on 21 April 2022. Downloaded on 8/26/2025 12:40:34 AM.
This article is licensed under a Creative Commons Attribution 3.0 Unported Licence.

31 L. Pang and F. Brisse, *J. Phys. Chem.*, 1993, **97**, 8562–8563.
32 P. Pyykkö, C. Wang, M. Straka and J. Vaara, *Phys. Chem. Chem. Phys.*, 2007, **9**, 2954–2958.
33 C. Wang, M. Straka and P. Pyykkö, *Phys. Chem. Chem. Phys.*, 2010, **12**, 6187–6203.
34 F. Cimpoesu, S. Ito, H. Shimotani, H. Takagi and N. Dragoe, *Phys. Chem.*, 2011, **13**, 9609–9615.
35 B. Frecus, C. M. Buta, C. I. Oprea, A. Stroppa, M. V. Putz and F. Cimpoesu, *Theor. Chem. Acc.*, 2016, **135**, 133.
36 S. Jalife, J. Arcudia, S. Pan and G. Merino, *Chem. Sci.*, 2020, **11**, 6642–6652.
37 M. S. Syamala, R. J. Cross and M. Saunders, *J. Am. Chem. Soc.*, 2002, **124**, 6216–6219.
38 N. Dragoe, A. M. Flank, P. Lagarde, S. Ito, H. Shimotani and H. Takagi, *Phys. Rev. B: Condens. Matter Mater. Phys.*, 2011, **84**, 155448.
39 E. K. Campbell, E. S. Reedy, J. Rademacher, R. J. Whitby and G. Hoffman, *Astrophys. J.*, 2020, **897**, 88.
40 S. Patchkovskii and W. Thiel, *J. Chem. Phys.*, 1997, **106**, 1796–1799.
41 G. R. Bacanu, T. Jafari, M. Aouane, J. Rantaharju, M. Walkey, G. Hoffman, A. Shugai, U. Nagel, M. Jiménez-Ruiz, A. J. Horsewill, S. Rols, T. Rõõm, R. J. Whitby and M. H. Levitt, *J. Chem. Phys.*, 2021, **155**, 144302.
42 W. H. Shaffer, *Rev. Mod. Phys.*, 1944, **16**, 245–259.
43 S. Flügge, *Practical Quantum Mechanics*, Springer-Verlag, Berlin, 1971, vol. 1.
44 C. Cohen-Tannoudji, B. Diu and F. Laloë, *Quantum Mechanics*, John Wiley & Sons, 2005.
45 D. A. Varshalovich, A. N. Moskalev and V. K. Khersonskii, *Quantum Theory of Angular Momentum*, World Scientific, 1988.
46 R. N. Zare, *Angular Momentum*, John Wiley & Sons, Inc., 1988.
47 D. L. Dexter, *Phys. Rev.*, 1956, **101**, 48–55.
48 C. C. Homes, P. J. Horoyski, M. L. W. Thewalt and B. P. Clayman, *Phys. Rev. B: Condens. Matter Mater. Phys.*, 1994, **49**, 7052–7055.
49 A. Shugai, U. Nagel, Y. Murata, Y. Li, S. Mamone, A. Krachmalnicoff, S. Alom, R. J. Whitby, M. H. Levitt and T. Rõõm, *J. Chem. Phys.*, 2021, **154**, 124311.
50 B. Meier, S. Mamone, M. Concistrè, J. Alonso-Valdesueiro, A. Krachmalnicoff, R. J. Whitby and M. H. Levitt, *Nat. Commun.*, 2015, **6**, 8112.
51 S. L. Altmann and P. Herzig, *Point-Group Theory Tables*, University of Vienna, Vienna, 2nd edn, 2011.
52 W. I. F. David, R. M. Ibberson, T. J. S. Dennis, J. P. Hare and K. Prassides, *Europhys. Lett.*, 1992, **18**, 219–225.
53 P. A. Heiney, *J. Phys. Chem. Solids*, 1992, **53**, 1333–1352.
54 P. M. Felker, V. Vlček, I. Hietanen, S. FitzGerald, D. Neuhauser and Z. Bačić, *Phys. Chem. Chem. Phys.*, 2017, **19**, 31274–31283.
55 C. Beduz, M. Carravetta, J. Y.-C. Chen, M. Concistré, M. Denning, M. Frunzi, A. J. Horsewill, O. G. Johannessen, R. Lawler, X. Lei, M. H. Levitt, Y. Li, S. Mamone, Y. Murata, U. Nagel, T. Nishida, J. Ollivier, S. Rols, T. Rõõm, R. Sarkar, N. J. Turro and Y. Yang, *Proc. Natl. Acad. Sci. U. S. A.*, 2012, **109**, 12894–12898.
56 K. S. K. Goh, M. Jimenez-Ruiz, M. R. Johnson, S. Rols, J. Ollivier, M. S. Denning, S. Mamone, M. H. Levitt, X. Lei, Y. Li, N. J. Turro, Y. Murata and A. J. Horsewill, *Phys. Chem. Chem. Phys.*, 2014, **16**, 21330–21339.
57 B. Sundqvist, *Adv. Phys.*, 1999, **48**, 1–134.

 This journal is © the Owner Societies 2022